Vol 4 (2) (2023)

Measurement, control and automation

Website: https:// mca-journal.org

ISSN 1859-0551

Computation of Electromagnetic Parameters of Shunt Reactors Taken Corner Chamfers of Core Blocks into Account

Hung Bui Duc[1], Dung Dang Chi[1], Vuong Dang Quoc[1] and Anh Hoang[1*]

[1]*School of Electrical Engineering, Hanoi University of Science and Technology*
[*]*Corresponding author E-mail: anh.hoang@hust.edu.vn*

Abstract

The shunt reactor (SR) is applied in electrical systems to avoid the overvoltage and absorb the reactive power in transmission lines under operation with no or low load conditions. To avoid magnetic saturation, an air gap is designed at the middle of core of SR. However, the size and shape of air gap will influence directly in the distribution of leakage and fringing fluxes. This leads to uneven distribution of flux density in the SR core and generate electromagnetic forces (EMFs) acting on the core and windings of the SR. The (EMFs) tend to push/compress the SR core with the different directions, causing oscillation, vibration, and generating audible noise, affecting the operation of the SR. Recently, many papers have studied the SR with one or several air gaps. For the one air gap, it usually has a large size, which leads to a significant leakage and fringing fluxes. In the case of multiple air gaps, the leakage and fringing fluxes will be smaller, leading to reduction of the EMF acting on the core blocks of SR. However, the use of multiple air gaps will encounter technological difficulties. In this paper, the corner chamfer of SR core is proposed to investigate the distribution of magnetic fields along the core block and EMF acting on the core block, as well. This development is performed with two steps: an analytical model is first presented to define main parameters of SR, then a finite element method is applied to calculate and simulate the electromagnetic parameters such as magnetic fields and electromagnetic forces of the SR. The presented method will be validated on a practical single-phase SR.

Keywords: *Shunt reactor, Core block, Magnetic field, Electromagnetic force, Analytical method, Finite element method.*

Symbols

Symbols	Units	Description
A	Wb/m	Magnetic vector potential
B	T	Magnetic flux density
H	A/m	Magnetic flux intensity
E	V/m	Electric field
J_s	A/m^2	Electric current intensity
μ	H/m	Magnetic permeability
σ	S/m	Electric conductivity
σ	S/m	Electric conductivity
Ω	.	Study domain
Ω_c		Conducting region
Ω_c^C		Non conducting region
$H^1(\text{curl};\Omega)$		Function space
$(\cdot,\cdot)_\Omega$		Volume integral
$<\cdot,\cdot>_\Gamma$		Surface integral

Abbreviations

SRs	Shunt reactors
FEM	Finite element method

1. Introduction

In order to avoid the overvoltage and maintain the stable voltage at the end of transmission lines of 110 kV, 220 kV and 500 kV under non-load or no-load operation, a shunt reactor (SR) is used to absorb and balance the reactive power [1]-[5]. Recently, many papers used different methods to study the SR with one or several air gaps. In [1], the SR with one air gap usually has a large size, which leads to a significant leakage and fringing fluxes as pointed out in Figure 1. This development was based on the Schwarz-Christoffel transformation [1] and 2D finite element analysis to investigate the field distribution around the air gap.

In [2], the SR with multiple air gaps was presented. In this study, the leakage and fringing fluxes will be smaller, reducing the electromagnetic force (EMF) acting on the core blocks of SR. However, the use of multiple air gaps will encounter technological difficulties. In [3], an analytical method was developed to compute the circuit dimensions and winding parameters of SR. The results obtained from the proposed method were verified by the finite element method (FEM). In [4], the authors applied the FEM to reduce losses caused by eddy currents in the winding of SR by optimizing the air gap clearance in the winding. The approach of the method was carried out in two steps: the calculation of the losses generated in the

Received: 10 May 2023; Accepted: 13 June 2023

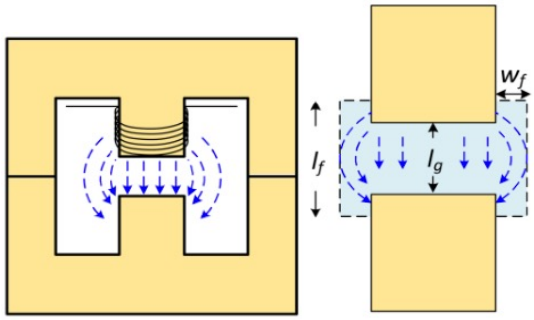

Figure 1. Modeling of the SR with an air gap [1].

winding is first considered. The average magnetic flux density around the air-gap is then computed. In [5], the authors presented a way of the air gap arrangements along the core blocks to reduce the influence of fringing fluxes around the air gaps. In, a FEM was developed to compute the field distributions around the air gaps, and the EMF on the core blocks of the SR.

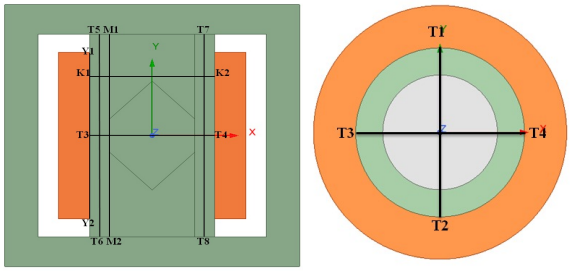

Figure 2. SR with air gap chamfer.

In this study, the air gap with different chamfers of SR core is proposed as shown in Figure 2. This development is performed with two steps: an analytical model is first presented to define main parameters of SR, and then a FEM is applied to investigate and simulate the distribution of magnetic fields along the core block and EMF acting on the core, as well. The proposed method will be validated on a practical single-phase SR ($Q = 16MVar$; $U = 500/\sqrt{3}$).

2. Background of theory

2.1. Electromagnetic problem by analytic analysis

As presented in [6]-[10], the electric current is defined via the relation of FEM, magnetic flux and magnetic reluctance, that is

$$I = (\frac{1}{\sqrt{2}})\frac{B_m.l_g}{\mu_0.N}, \tag{1}$$

where B_m is the maximum magnetic flux density in the core (T), l_g is the air gap length (m), N is the turn numbers of the winding and μ_0 is the permeability of the air gap H/m. The B_m is calculated via the below expression [6]:

$$B_m = \sqrt{\frac{Q.\mu_0}{\pi.f.V_g}}, \tag{2}$$

where Q is the reactive power of SR (MVar), f is the frequency and V_g is the air gap volume (m^3). Based on the value of magnetic flux density defined in (2), the EMF (F) acting on the SR core is defined [7], [8], i.e.,

$$F = \frac{1}{2}\frac{B_m^2}{\mu_0}S_c\,(N) \tag{3}$$

where S_c is the cross-section of the SR core (m^2). From the (3), the EMF density acting on the core surface is defined as

$$F_s = \frac{F}{S_c} = \frac{1}{2}\frac{B_m^2}{\mu_0}\,(N/m^2) \tag{4}$$

In addition, the F_s can be defined via the Maxwell stress tensor, that is [5], [16]

$$F_s = -\frac{1}{2}H.\bigtriangledown B = -\frac{1}{2}H.H\bigtriangledown\mu\,(N/m^2) \tag{5}$$

The term of F_s can be defined via the normal and tangential components

$$F_s = -\frac{1}{2}(H_n^2+H_t^2)\bigtriangledown\mu = -\frac{1}{2}(\frac{B_n^2}{\mu^2}+H_t^2)\bigtriangledown\mu\,(N/m^2) \tag{6}$$

If the fringing flux is neglected, the the tangential component (H_t) is equal to zero. Thus, the equation (6) becomes

$$F_s = -\frac{1}{2}(\frac{B_n^2}{\mu^2})\bigtriangledown\mu\,(N/m^2) \tag{7}$$

2.2. Electromagnetic problem with the FEM

In this part, the FEM is developed to analyzed electromagnetic parameters of the SR. Where the EMF (F) acting on the core blocks is performed via the post-processing. The set of Maxwell's equations defined in Ω ($\Omega = \Omega_c \cup \Omega_c^C$ is written as [5], [11]-[13]:

$$\mathrm{curl}\,H = J_s\,,\ \mathrm{div}\,B = 0\,,\ \mathrm{curl}\,E = -\partial_t B \tag{8a-b-c}$$

These equations are solved with the behavior laws, i.e.,

$$B = \mu H, J = \sigma E \tag{9a-b}$$

The boundary conditions (BCs) are then expressed as

$$n\cdot B|_{\Gamma_e} = 0\,,\ n\times H|_{\Gamma_h} = 0\,, \tag{10a-b}$$

where n is the normal component.
Besed on the set of Maxwells equations and behavior laws given in (8) and (9a-b), the term on B is expressed via the A, that is

$$B = \mathrm{curl}A \tag{11}$$

By substituting (11) into (9a-b a), one has

$$\mathrm{curl}\,(E + j\omega A) = 0 \tag{12}$$

The weak form for magnetic vector potential formulations (A) is established via the Ampere law (8 a)

$$(\mu^{-1}\mathrm{curl}A, \mathrm{curl}A')_\Omega + (\sigma E, A')_{\Omega_c} + \langle n\times H, A'\rangle_{\Gamma_h}$$
$$= (J_s, A')_{\Omega_s}, \forall A' \in H_h^1(\mathrm{curl};\Omega) \tag{13}$$

Table 1. Main parameters of the SR

No	Parameter	Symbol	Value
1	Reactive power	$Q(MVAr)$	16
2	Rated voltage	$U(kV)$	$500/\sqrt{3}$
3	Rated voltage	$U(kV)$	$500/\sqrt{3}$
4	Total inductance	$L(H)$	16,57
5	Fringing inductance	$L_f(H)$	5,15
6	Air gap inductance	$L_{air}(H)$	10,26
7	Core diameter	$D_s(m)$	0.572
8	Core height	$H_s(m)$	1,534
9	Core height	$H_s(m)$	1,534
10	Length of air gap	$l_k(m)$	0.256
11	Turn numbers	$N(turn)$	2853
12	Winding width	$W_d(mm)$	0.211
13	Winding heigth	$H_d(mm)$	1.264

The E in (13) is expressed via the magnetic scalar potential (v), that is $E = -j\omega A - \text{grad}\, v$. Thus, the equation (13) is rewritten as [16]:

$$(\mu^{-1}\text{curl}A, \text{curl}A')_\Omega + (\sigma A, A')_{\Omega_c} + j\omega(\sigma \text{grad}\, v, A')_{\Omega_c} + \langle n \times H, A' \rangle_{\Gamma_h} = (J_s, A')_{\Omega_s}, \forall A' \in H_h^1(\text{curl}; \Omega) \quad (14)$$

The EMF (F) acting on the core blocks is now defined via the post-processing, i.e.,

$$F = \int_{\Gamma_{block}} \text{curl}A \times J \cdot d\Gamma_{block} = \int \Gamma_{block} B \times J \cdot d\Gamma_{block} \quad (15)$$

where Γ_{block} is the surface of core block.

3. Application test

To verify the developed theoretical model, the practical application problem is a practical single-phase SR. The main parameters of the SR obtained by the analytical method are given in Table 1. The geometric structure of the SR with a chamfer corner of 45^0 is already described in Figure 1. The 3D mesh of the SR to achieve convergence of the solution is presented in Figure 3.

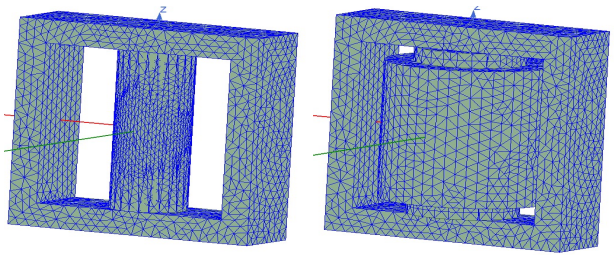

Figure 3. 3D mesh of the SR.

The distribution of fields (such as the magnetic vector potential and magnetic field) is pointed out in Figure 4. Figure 5 and Figure 6 show the comparison of distribution of magnetic flux density (B) in the air gap of SR along the $T1T2$ and $T3T4$, for different chamfer corners with the reference solution. In the case of an air gap with no chamfer corner, the results indicate that for the $T1T2$ axis, the B reaches its maximum value ($B = 0.34T$) in the middle region of the core and decreases sharply towards the edges of the core . At the $T3T4$ axis position, the B value reaches $0.78T$ (reaching saturation) and decreases to $0.35T$ in the edge region of the core (air gap), due to the higher magnetic reluctance in this region compared to the center position of the core. In the case of different chamfer corners, the B in the middle of the core decreases significantly and gradually increases towards the edges of the core, while decreasing gradually from the edges towards both sides. It should be noted that the value on B is the smallest in comparison with the smaller chamfer corners and reference. The distribution of B along the winding height (T5 and T6; T7 and T8), for the different chamfer corner is presented in Figure 7. In a similar way to the previous explanation, the value on B is the lowest for the chamfer corner of 45^0 and is the biggest for the air gap with no chamfer corner.

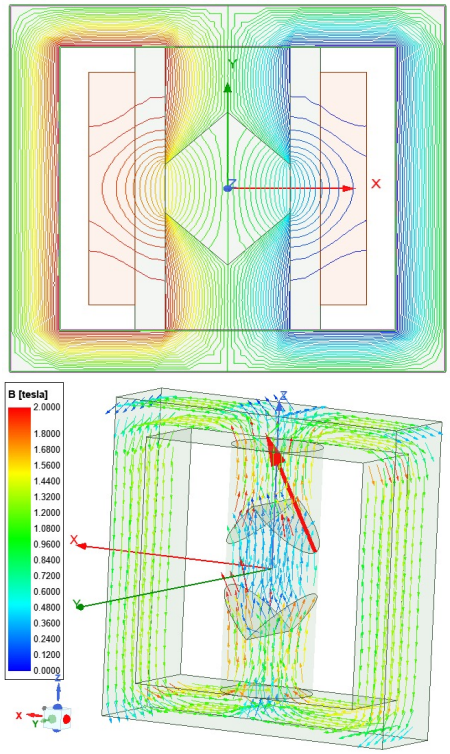

Figure 4. Distribution of magnetic vector potential (*left*) and magnetic field (*right*), for chamfer corner of 45^0.

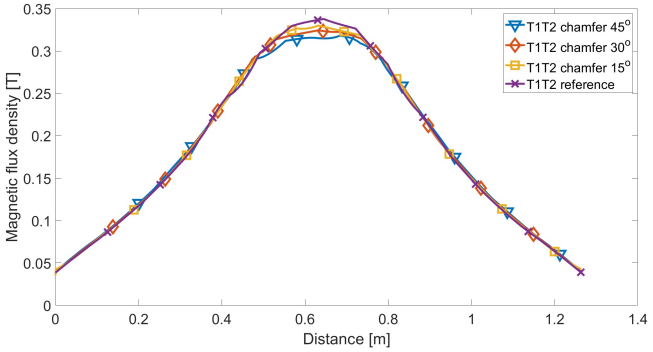

Figure 5. Distribution of magnetic flux density in the air gap of SR along the T1 and T2, for different chamfer corners.

Figure 8 illustrates the distribution of B along the height of the core (M1M2). For the air gap with no chamfer corner, the

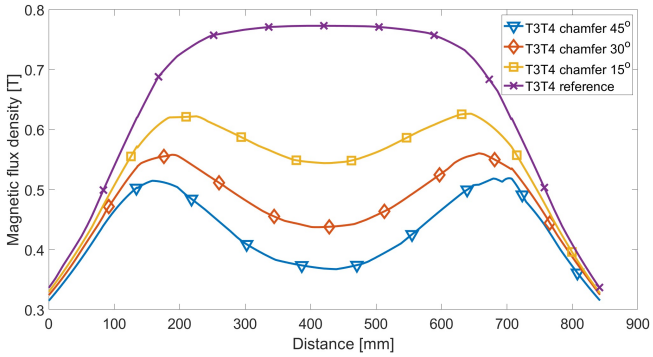

Figure 6. Distribution of magnetic flux density in the air gap of SR along the T3 and T4, for different chamfer corners.

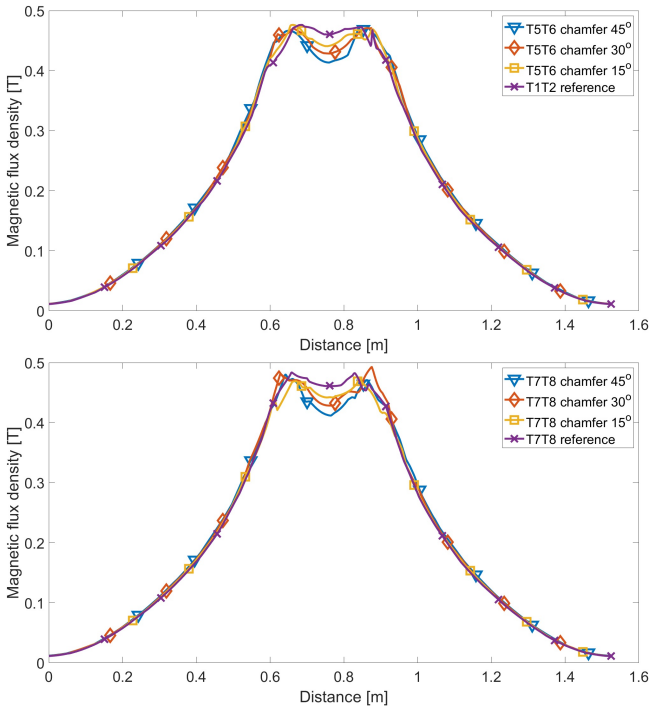

Figure 7. Distribution of magnetic flux density along the winding height (T5 and T6; T7 and T8), for different chamfer corners.

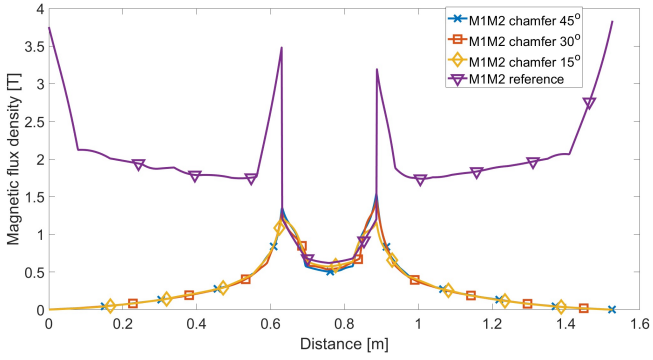

Figure 8. Distribution of magnetic flux density in the air gap of SR along the M1 and M2, for different chamfer corners.

result shows that along the winding, the B is relatively low due to the higher magnetic reluctance.

Figure 9 illustrates the distribution map of the EMF (F) for a chamfer corner of 45^0. In Figure 10, it can be observed that the EMFs have the same direction but opposite in magnitude, exerting a pushing and squeezing effect on the core along the air

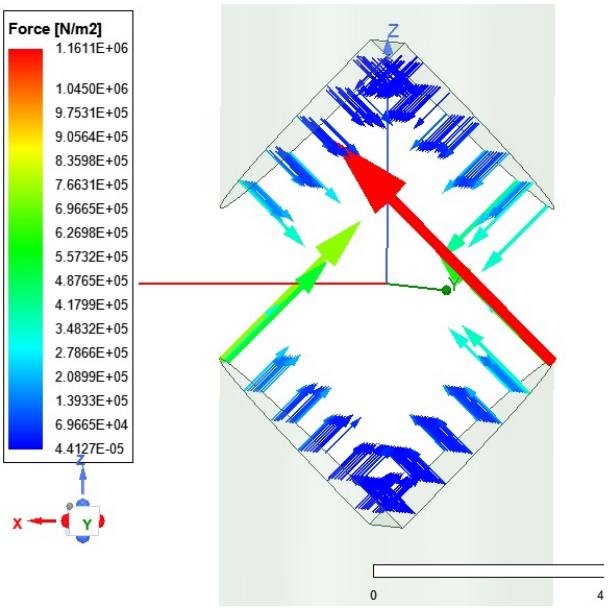

Figure 9. Distribution of electromagnetic force for a chamfer corner of 45^0.

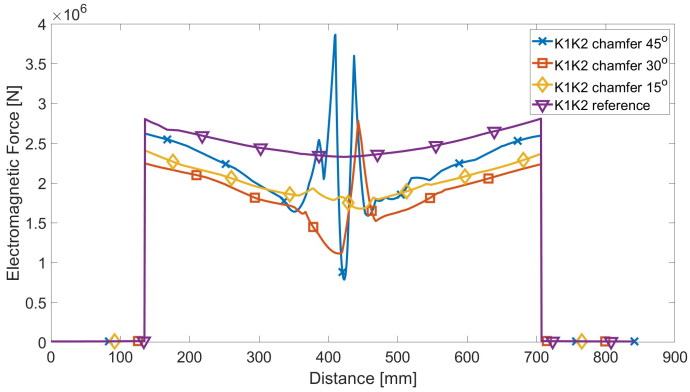

Figure 10. Distribution of electromagnetic force in the air gap of SR along the K1 and K2, for different chamfer corners.

gap. This can cause a misalignment of the core, affecting the structure of the electromagnetic circuit and generating noise during operation. In the case of a chamfered air gap, the EMFs along the $K1K2$ section exhibit fluctuations in the middle of the core. It should be noted that the evenly distributed the EMF corresponds to the case of a chamfered air gap at a 15^0. With a chamfer the corner of 115^0, the flux leakage and fringing flux reach the minimum value as the analyzed above.

4. Conclusion

In this paper, the two methods (analytical method and FEM method) have been successfully presented for computing and simulating the magnetic flux density distribution inside and around the air-gap of the core blocks and the EMFs) acting on the surface of the core blocks of the SR. In both methods, the obtained results have showed that the EMF acting on the upper and lower surfaces of the core block is in the same direction but opposite in magnitude, approximately equal to each other. This directly affects the separating plates between the core blocks, causing structural deformation of the core blocks and winding due to the high compressive force they have to

endure. The results obtained from this study will serve as a basis to help designers and manufacturers of SRs to develop solutions for the structure of the separating plates between the core blocks prior to production. Particularly, it provides the appropriate choice of the chamfer corner in the steel core to reduce the EMF acting on the surface of the core blocks and the surfaces of the separating plates with the different chamfer corner. In particular, the paper has presented the electromagnetic fields with the chamfer corners of 15^0, 30^0 and 45^0, where the suitable chamfer corner for the core block is 30^0. Based on this analysis, it will help the designer and manufacture to improve electromagnetic parameters of the SR.

References

[1] L. M. Escribano, R. Prieto, J. A. Oliver, J. A. Cobos, and J. Uceda (2002). *New modeling strategy for the fringing energy in magnetic components with air gap.* APEC. Seventeenth Annual IEEE Applied Power Electronics Conference and Exposition (Cat. No.02CH37335), vol. 1, pp. 144150, 2002, doi: 10.1109/APEC.2002.989240.

[2] T. P. Minh, H. B. Duc, and V. D. Quoc (2022). *Analysis of Leakage Inductances in Shunt Reactors-Application to High Voltage Transmission Lines.* Eng. Technol. Appl. Sci. Res., vol. 12, no. 3, pp. 84888491.

[3] Gagari Deb (2012). *Ferranti Effect in Transmission Line.* International Journal of Electrical and Computer Engineering, Vol.2, No.4, pp. 447-451.

[4] A. Divya Swarna Sri (2018).

[5] Pham Minh, T. (2021). *Computation and Simulation of Shunt Reactor by an Analytical method and Finite element Method-Application to transmission lines of high and super high voltages.* Journal of Military Science and Technology, no. 74, pp. 36-43. *Depiction and Compensation of Ferranti Effect in Transmission Line.* International Journal for Research in Applied Science & Engineering Technology, Volume 6 Issue III.

[6] H. Amreiz, A. Janbey and M. Darwish (2020). *Emulation of Series and Shunt Reactor Compensation.* 55th International Universities Power Engineering Confer-ence (UPEC), pp. 1-6, doi: 10.1109/UPEC49904.2020 .9209786.

[7] Bui Duc Hung, Dung Dang Chi, Do Chi Phi, & Dang, Q.-V. (2023). *Studying the influence of electromagntiec forces on core blocks of the shunt reactors by using the analytical model and finite element approach.* Measurement, Control, and Automation, 4(1), 44-48. https://mca-journal.org/index.php/mca/article/view/167.

[8] D. I. Zaikin, S. Jonasen and S. L. Mikkelsen (2019). *An Air-Gap Shape Optimization for Fringing Field Eddy Current Loss Reductions in Power Magnetics.* In IEEE Transactions on Power Electronics, vol. 34, no. 5, pp. 4079-4086, May 2019, doi: 10.1109/TPEL.2018.2868289.

[9] A. Balakrishnan, W.T. Joines, T.G. Wilson (1997). *Air-gap reluctance and inductance calculations for magnetic circuits using a Schwarz-Christoffel transformation.* IEEE Transactions on Power Electronics vol. 12, pp. 654663.

[10] Lự, Fangcheng & Guo, Jiayi & Niu, Leilei & Geng, Jianghai & Pan, Yirui (2019). *A New 3D Method for Reactor Core Vibration Based on Silicon Steel Lamination Rules and Application in UHV Shunt Reactors.* Math-ematical Problems in Engineering. 2019. 1-11. 10.1155/2019/72 90536.

[11] S.V. Kulkarni, S.A. Khaparde (2012). *Transformer Engineering: Design, Technology, and Diagnostics.* Second Edition, ISBN 9781439853771, Published October 10, 2012 by CRC Press.

[12] S. Koruglu, P. Sergeant, R.V. Sabarieqo, Vuong. Q. Dang, M. De Wulf (2012). *Influence of contact resistance on shielding efficiency of shielding gutters for high-voltage cables.* IET Electric Power Applications, Vol.5, No.9, (2011), pp. 715-720.

[13] Najafi, A., Iskender, I. (2018). *Comparison of core loss and magnetic flux distribution in amorphous and silicon steel core transformers.* Electr Eng 100, 11251131 (2018). doi:10.1007/s00202-017-0574-7.

[14] K. Dawood, G. Komurgoz and F. Isik (2019). *Modeling of Distribution Transformer for Analysis of Core Losses of Different Core Materials Using FEM.* 2019 8th International Conference on Modeling Simulation and Applied Optimization (ICMSAO), 2019, pp. 1-5, doi: 10.1109/ICMSAO.2019.8880392.

[15] K. Dawood, G. Komurgoz and F. Isik (2020). *Evaluation of the Electromagnetic Forces in the Shunt Reactor by using Finite Element Analysis.* International Conference on Electrical Engineering (ICEE), pp. 16, doi: 10.1109/ICEE49691.2020.9249871.

[16] A. Y. Arabul, E. Kurt, F. Keskin Arabul, and . enol (2020). *Modelling of the equally distributed air gapped shunt reactor.* Pamukkale University Journal of Engineering Sciences, vol. 26, no. 2, pp. 286294, doi: 10.5505/pajes.2019.95826.